International Journal of Heat and Mass Transfer 52 (2009) 1643–1656

Contents lists available at ScienceDirect

International Journal of Heat and Mass Transfer

journal homepage: www.elsevier.com/locate/ijhmt

A study on slow evaporation of liquids in a dual-porosity porous medium using square network model

K.M. Pillai [a,*], M. Prat [b], M. Marcoux [b]

[a] Department of Mechanical Engineering, University of Wisconsin-Milwaukee, EMS Bldg., 3200 N. Cramer St., Milwaukee, WI 53211, USA
[b] Institut de Mécanique des Fluides de Toulouse, U.M.R. C.N.R.S. – INP/UPS N°5502, Allee du Pr. Camille Soula, 31400 Toulouse, France

ARTICLE INFO

Article history:
Received 17 June 2008
Received in revised form 8 October 2008
Available online 11 December 2008

Keywords:
Drying
Porous media
Dual-porosity porous media
Dual-scale porous media
Invasion percolation
Films

ABSTRACT

Slow evaporation of a liquid is studied in a two-dimensional pore square network of aspect ratio 1 with three sides insulated and one side exposed to air for drying. In this study, the external transfer resistance and liquid-film effects are ignored while the capillary effects dominate viscous and gravity forces in the hydrophilic network. The square domain is divided into two layers with distinct porosities and particle sizes such that the two layers are exposed to drying alternately. A 100×100 network simulation of two cases of the exposed larger-pore layer shielding the smaller-pore layer, and the exposed smaller-pore layer shielding the larger-pore layer, lead to dramatically different responses in terms of the liquid evaporation plots and saturation distributions. The former case retains moisture in the inner smaller-pore layer till the entire outer larger-pore layer is dry, and is characterized by decaying liquid evaporation plots. The latter case leads to loss of moisture in both the exposed smaller-pore layer (due to evaporation) and the inner larger-pore layer (due to capillary pumping), and is characterized by bilinear evaporation plots (with an initial faster evaporation followed by a subsequent slower one). A case study that imposes uniform porosity in the two layers but keeps particle sizes different in the two layers indicate that though the pattern of saturation distribution during evaporation may remain similar to the earlier cases, but the evaporation plots are significantly different. An experimental validation of the simulation is undertaken with the help of a smaller 12×12 network where saturation patterns and evaporation plots are replicated well by the simulation. However the presence of surface liquid films created due to surface roughness as well as the capillary-suction driven liquid redistribution may be the cause of the large mismatch in the drying time of the network.

1. Introduction

Evaporation in porous media is of significant interest in relation with many applications such as light oil recovery, soil remediation, water management in fuel cells, weathering of monuments and buildings, and of course drying, to name only a few. Although all these applications have motivated many research efforts in the past, numerous aspects of evaporation in a porous medium still need to be understood and clarified. Until the beginning of the nineties, the study of evaporation in a porous medium was addressed using mostly phenomenological approaches in which the porous medium was assumed to be a continuum of averaged physical quantities, e.g. [1]. To overcome the limitations of this type of approach in which the effect of porous microstructure is lumped into effective parameters, more recent works have focused on capturing the effect of pore geometry on evaporation dynamics through pore network models (see [2,3], for reviews of this growing field). A two-dimensional model taking into account capillary effects through an invasion percolation (IP) rule and the transport by diffusion in the gas phase of the evaporating species was proposed in [4]. Since this first model, increasingly sophisticated models have been developed to take into account gravity effects [5], viscous effects [6], thermal effects [7–9], liquid-film effects [10,11], and binary liquid effects [12]. Three-dimensional versions of the network model, though not including all effects, have also been developed [13–16]. Experiments with etched networks [17,18] have led to satisfactory validation of two-dimensional models in terms of drying patterns and have shown that liquid-film flows can have a strong influence on drying rates (see also [11]). The analysis of drying patterns can be performed using invasion percolation concepts and this has been performed in some details in [19,20], notably in relation with the experimental results reported in [21] which indicate that the viscous effects stabilize the invasion. These studies have been performed assuming a hydrophilic porous medium. The case of hydrophobic porous media was also considered recently [22]. From these studies, it emerges that drying in a hydrophilic porous medium is a drainage process that can be analyzed using the simple model proposed in [4], provided the drying is sufficiently slow for the thermal effects to be negligible (assuming the evaporation of li-

* Corresponding author. Tel.: +1 414 229 6535; fax: +1 414 229 6958.
E-mail address: krishna@uwm.edu (K.M. Pillai).

0017-9310/$ - see front matter © 2008 Elsevier Ltd. All rights reserved.
doi:10.1016/j.ijheatmasstransfer.2008.10.007

Nomenclature

a	inter-pore distance in network
F_c	net evaporation flux at cluster boundary
D	diffusion coefficient of water vapor in air
h	mass transfer coefficient; distance of effective drying front from interface (in Appendix)
H	length of small-pore region (in Appendix)
j	evaporation mass-flux
K	$(DM_v)/(RT)$
l	bond width
m_e	mass of evaporated water
m_e	water evaporation rate
M_v	molecular weight of water
P_v	partial pressure of water vapor in air
P_{atm}	atmospheric pressure
R	universal gas constant
t	time
t_c	evaporation time for the largest throat at a cluster boundary
T_{brk}	time to achieve breakthrough of air phase
V_l	volume of liquid contained in throat and adjacent pore
V_{sc}	volume of liquid contained in the largest throat at a cluster boundary at time t
β	network occupancy coefficient
δ	external (gas film) transfer length scale
ε	porosity
ρ_l	liquid density

Subscripts

e	at the effective drying front
i	at the interface
∞	in the surrounding air
L	corresponding to the large-pore region
S	corresponding to the small-pore region
min	minimum (bond width)
max	maximum (bond width)

quid to be occurring at room temperature, for example), and the liquid-film effects can be ignored.

All the cited studies have focussed on the modeling and understanding of drying phenomena in a microstructure which is a regular lattice, and in which the disordered nature of a porous medium is taken into account only through narrow monomodal random distributions of pore and throat sizes. Clearly, one of the major advantages of pore network models is to make possible the study of the effect of pore structure on drying. Hence, not surprisingly, several recent studies have concentrated on investigating the role of pore structure at different scales. At pore scale, the impact of pore shape was studied in [11–14], and was found to be very important in relation with the liquid-film transport phenomena. In [23], the impact of bimodal distribution was investigated in addition to monomodal distributions of various coordination numbers. In particular, it was shown that bimodal pore structures could have a great impact on drying kinetics. This type of study opens up a way of controlling the drying rate, i.e. for example the rate at which a volatile species is delivered to the surrounding atmosphere, by controlling the microstructure of the involved porous media.

Another important class of structural effects can be referred to as the macroscopic inhomogeneities or the large-scale heterogeneities. Such heterogeneities have a great impact on the invasion pattern in drying [24]. Since the invasion takes place preferentially in large pores, regions of larger pores tend to be invaded first whereas the regions of smaller pores are left liquid saturated much longer. Once again, this offers a way of controlling the drying rate. We also note that most of the naturally occurring porous media can be characterized as large-scale heterogeneous media even at the core scale. Stratified porous media can be considered as the archetypical large-scale heterogeneous porous media, and represent a natural first choice for studying the effect of large-scale heterogeneities on drying.

In this context, the objective of the present work is to study drying in two-layer porous media using the pore network model proposed in [4]. In passing we note that this two-layer configuration is for example encountered in the poulticing technique of desalination of porous media [25]. This model has been presented in many previous publications and therefore is only briefly summarized here. It combines the invasion percolation (IP) rules applied to each liquid cluster (the bond to be invaded in a cluster is the bond of largest width located at the periphery of the cluster) with a finite-volume type computation of the vapor partial-pressure field in the air invaded region, and thereby of the evaporation flux at the boundary of each cluster.

The paper is organized as follows. First a brief description of the network model as applied to the dual-porosity geometry as well as of the imposed condition will be provided. Later results of various case studies conducted with a large network will be discussed. Comparison with experimental results will be considered next. Finally the paper will be concluded with an outline of future work as well as a summary of important results.

2. Geometry of square network, initial and boundary conditions, drying algorithm

In this study, the porous medium is represented by a two-dimensional network of randomly sized pores joined by randomly sized throats. As shown in Fig. 1, the pores and the throats are located, respectively, at the nodes and bonds of a two-dimensional square lattice. The width l of each throat or bond is chosen randomly according to the uniform distribution law. The other important parameters deciding the porosity and pore structure are the inter-nodal distance a and the space distribution coefficient β.

A 100×100 network in a square domain as shown in Fig. 2 was selected for this study. The pores and nodes of the network are ini-

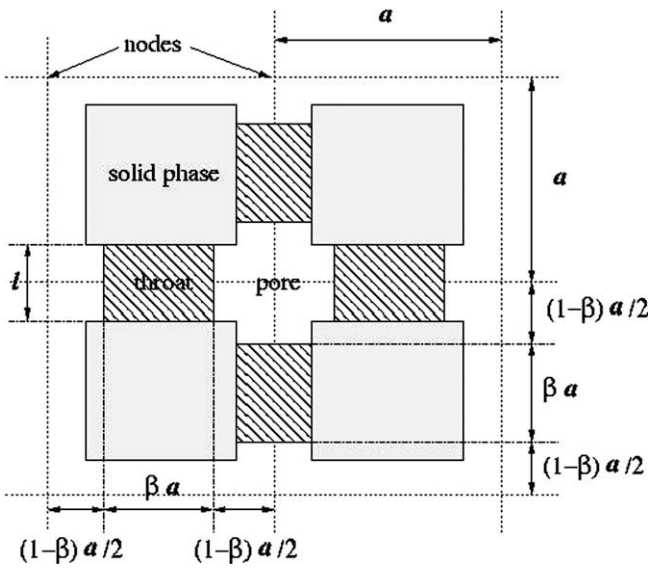

Fig. 1. Definitions and geometrical parameters of the network.

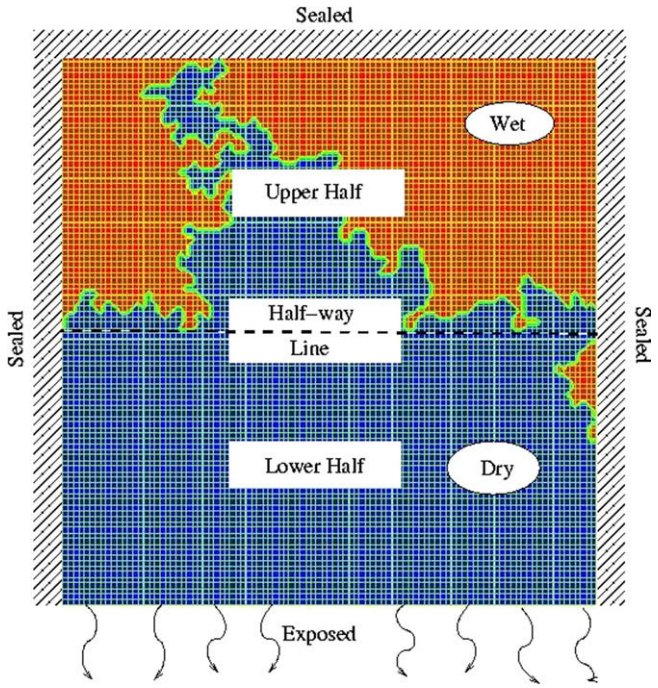

Fig. 2. A typical 100 × 100 dual-porosity network used for 2-D drying simulation. The rectangular domain is divided into upper and lower halves (or layers) with different porosities. The darker (blue) area represents the dried porous medium with air inside the pores, while the lighter (red) area signifies the wet porous medium with liquid residing in the pores. (For interpretation of color mentioned in this figure the reader is referred to the web version of the article.)

tially saturated with water, which is then allowed to evaporate isothermally from the randomly sized pores and bonds of the network. As we can see in the figure, the three upper sides of the square domain are sealed, i.e. they represent the impervious surfaces. The fourth lowermost side of the domain is open to air for drying. On this side, we use a standard mass-flux boundary condition of the form

$$j = h(P_{v,o} - P_{v,\infty}) \tag{1}$$

where j is the evaporation flux density, h is the mass transfer coefficient, $P_{v,o}$ vapor partial pressure at the porous medium surface, $P_{v,\infty}$ and is the vapor partial pressure in the surrounding air. The mass transfer coefficient h is expressed as

$$h = \frac{D}{(R/M_v)T\delta} \tag{2}$$

where D is the diffusion coefficient of water vapor, R is the universal gas constant, M_v is the vapor molecular weight, T is temperature, and δ is the external (gas film) transfer length-scale (see [11] for more details). Focusing on the structural impact, the external transfer resistance is specified so as to be negligible (i.e. $\delta << a$).

The main purpose of this section is to study changes in saturation patterns and evaporation rates if the upper and lower regions of the square domain have distinct pore sizes and porosities. For this purpose, the square domain is divided into two rectangular domains as shown in Fig. 2. One of them will be designated as the *larger pore-size* layer with bond width l distributed randomly between $0.7a$ and $0.8a$ where a (= 0.001 m) is the distance between two pores in the network (Fig. 1). The other region will be designated as the complimentary *smaller pore-size* layer with bond width l distributed randomly between $0.1a$ and $0.2a$. It is to be noted that the larger pore-size region will have a higher porosity as compared to the smaller pore-size region since the inter-nodal distance remains the same in the two layers. To construct one realization of the two-layer pore network, a random number p taken in the range [0,1] is assigned to each bond of the network. Then the width of each bond is computed as $l = l_{min} + (l_{max} - l_{min})p$, with $l_{min} = 0.7a$ and $l_{max} = 0.8a$ in the larger pore-size layer, and $l_{min} = 0.1a$ and $l_{max} = 0.2a$ in the smaller pore-size layer.

For the sake of completeness, the drying algorithm is summarized here (see [4] for more details): (1) every liquid cluster present in the network is identified, (2) the interfacial throat of greatest width is identified for each cluster and the volume V_{sc} of liquid contained at time t in this throat and the adjacent pore is estimated, (3) the evaporation flux F_c at the boundary of each cluster is computed from the finite-volume computation of the liquid vapor partial pressure in the gas phase, (4) the time t_c required to evaporate the amount of liquid contained in the interfacial throat identified in step 2 is computed as $t_c = \frac{\rho_\ell V_{sc}}{F_c}$ for each cluster, (5) the throat, among the throats selected in step 2 and which is eventually invaded, corresponds to $t_{cmin} = \min(t_c)$, (6) the phase distribution within the network is updated, which includes the partial evaporation of liquid contained in the throats selected in step 2 using $\rho_\ell V_\ell(t + t_{cmin}) = \rho_\ell V_\ell(t) - F_c t_{cmin}$ (where ρ_ℓ is the liquid density and V_ℓ the volume of liquid contained in the throat + adjacent pore) except for the throat selected in step 5 (as well as the adjacent pore) which becomes completely saturated by the gas phase. The procedure can be repeated up to full drying of the network or stopped at some intermediate stage.

3. Results and discussion

3.1. Simulation studies on the dual-porosity pore network model

3.1.1. Case 1: smaller pores outside, larger pores inside

Here, we will study the evaporation from a porous medium consisting of larger pores that is covered with a porous layer made of smaller pores. This is achieved in our simulation by considering the lower half of the domain as the smaller pore-size region while the upper half is recreated as the larger pore-size region.

The evolution of phase distribution is shown in Fig. 3. The phase distribution in the beginning resembles similar distributions for a regular, homogeneous network, e.g. as seen in [17]. The breakthrough (i.e. when the air phase, region represented by a darker color, manages to traverse the length of the network, and reaches the side opposite to the exposed side) happens after 24.7 h. After the breakthrough, one can notice a large build-up of air phase distribution beyond the boundary in the large-pore region. Explanation is as follows. Note that the empty larger pores shown in Fig. 3d have a very 'small neck' connection with the outside air through the empty smaller pores. As a result, the evaporation in the larger pores will be quite small as relative humidity in these 'locked' larger pores is expected to be close to 1 (this phenomenon is referred to as the diffusional screening process). So the 'emptying' of bigger pores witnessed in part d is not due to evaporation from the menisci located in the large-pore region. As sketched in Fig. 4, the evaporation is significant only in the small-pore region at this stage of drying. Hence the emptying of pores in the large-pore region is in fact due to the transport of the liquid phase through clusters spanning over both the small-pore and the large-pore regions (Fig. 4). According to the drying algorithm described in Section 2, large pores are preferentially invaded since they have smaller capillary pressure thresholds. Hence as long as a cluster spans over the two regions, interfacial throats located in the large-pore region are preferentially selected for drainage due to their lower capillary pressure thresholds. As sketched in Fig. 4, this *implies* capillary pumping from the large-pore region to the small-pore region, even though such a liquid flow is not modeled explicitly by the IP algorithm. The boundary of the biggest cluster in the small-pore region remains virtually unchanged through parts (c) and (d) of Fig. 3 in agreement with this assertion. As for

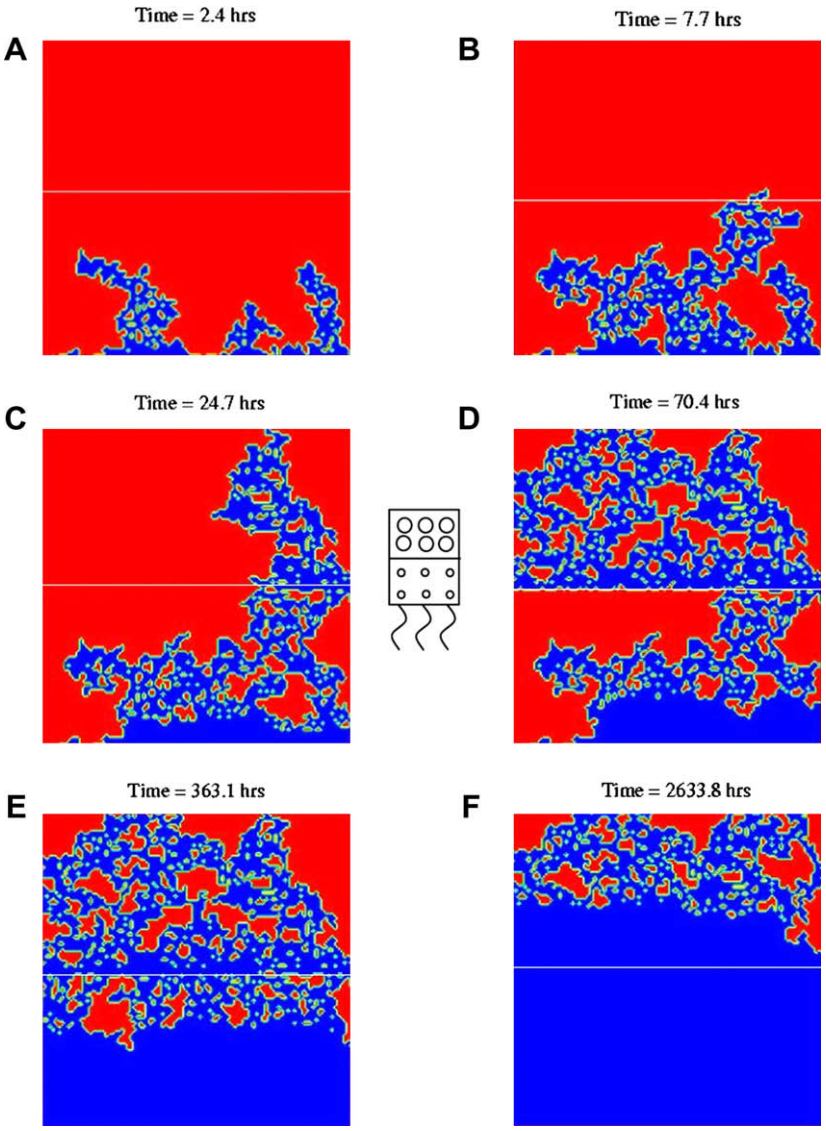

Fig. 3. A typical evolution of drying in a 100 × 100 dual-porosity network with small pores in the bottom exposed layer. Evaporation happens at the bottom edge of the square; the other edges are sealed. Part (C) shows the state of pore saturation at the 'breakthrough'.

an ordinary invasion percolation process, the phenomenon of breakup of a single cluster into several smaller clusters happens in case of the large-pore upper layer. This effect is clearly visible in the upper layer shown in Fig. 3d: the large liquid cluster spanning the middle interface on the left hand side (Fig. 3c) splits up into several smaller clusters in the upper layer. As a result of cluster breakup mechanism into the large-pore region, the clusters in this region eventually cease to be hydraulically connected to the small-pore regions. As a result, we expect the invasion in the large-pore region to cease for a while when there are no liquid clusters spanning over the two regions anymore. This can indeed be seen happening from Fig. 3d and e. Fig. 3d shows the phase distribution with no liquid cluster spanning across the interface between the two regions. Fig. 3e clearly shows that the saturation distribution in the large-pore region remains virtually unchanged while rapid evaporation is seen in the small-pore region marked by the development of a dry region on the side of the exposed lower edge. By 2633.8 h (part f), this dry zone has crossed the boundary, and has progressed into the large-pore region. The farther the drying front moves from the exposed lower edge, the longer it takes to dry, as the vapor-diffusion resistance increases with distance of the front from the exposed edge.

3.1.2. Case 2: larger pores outside, smaller pores inside

Let us now study a case when a porous medium consisting of smaller pores is covered with layer of porous material made of larger pores. This is achieved in our simulation by considering the lower half of the domain as the large-pore region while the upper half is recreated as the small-pore region.

The evolution of phase distribution for this 'reverse' case is presented in Fig. 5. A very striking observation about this case is that for around 500 h, the evaporation is happening entirely within the larger pores-so much so that we have a completely wet inner region of smaller pores surrounded by a completely dry outer region of larger pores (see part (d) of Fig. 5) Moreover the breakthrough here happens at 672.5 h, much later than the breakthrough time of 24.7 h observed in Case 1 considered earlier.

We also observe that the smaller pores do not start emptying until all the larger pores are empty—this is quite natural since any drying interface that is in touch with both the large and small throats (as in part c) will lead to emptying of larger throats first as they have a larger invasion potential in the invasion percolation algorithm. (In accordance with the drying algorithm described in Section 2, the invasion potential of a bond can be defined here as being proportional to its width since the capillary pressure thresh-

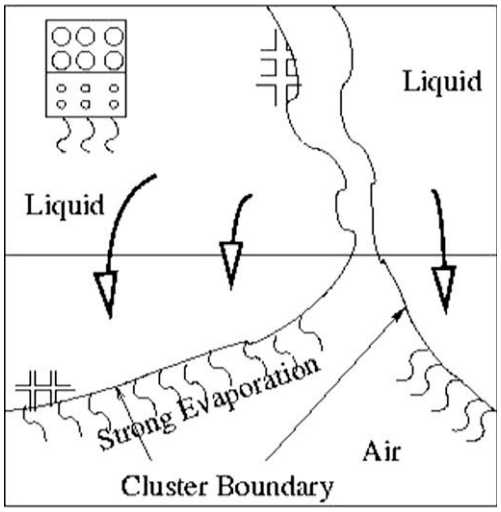

Fig. 4. Pumping of liquid happens from the upper layer with larger pores to the lower layer with smaller pores in liquid clusters spanning the middle interface of any dual-porosity network. The 'breakthrough' in the upper layer creates two such clusters. The saturation in the upper layer decreases as the single unified liquid cluster splits into several isolated clusters in the upper layer as a result of this pumping action driven due to the higher capillary pressures in the smaller pores as well as the stronger evaporation in the lower part of the clusters.

old to overcome for invading a bond is inversely proportional to the bond width according to Laplace law; see [4] for more details.) So clearly, the water saturation in the inner small-pore region is preserved for a longer time due to the preferential evaporation of water in the larger pores. In other words, a 'protective covering' of the large-pore outer region keeps the inner small-pore inner region wet longer.

3.2. Effect of random alterations in the pore structure

Since our network is generated by assigning throat widths randomly between certain ranges in the two layers, it is not prudent on our part to ignore the effect of such randomness in network realizations on the evaporation phenomenon. So for the two cases of the exposed large pores and the exposed small pores, we decided to study the effect of various network realizations on the evaporation patterns and phase distributions.

3.2.1. Variations in breakthrough pattern

Breakthrough of air phase to the inner boundary during evaporation forms an important milestone in the evaporation of liquids in any porous medium. For the exposed large pores case, the breakthrough time (T_{brk}) varied from 672.5 to 918.7 h with an average T_{brk} of 788.5 h and a standard deviation of 75.6 h in six different network realizations. For the exposed small-pores case, a larger scatter in T_{brk} from a low of 24.7 h to a high of 508 h with an average of 196 h and a standard deviation 167 h was observed in five different network realizations. So the exposed smaller pores achieve much faster breakthrough as compared to the exposed larger pores.

3.2.2. Scatter in the evaporated mass versus time curves

For the two cases of the exposed large pores and the exposed small pores, we decided to study the effect of various network realizations on rates of liquid evaporation. Fig. 6, which plots the mass of liquid evaporated m_e against elapsed time t, describes such a study for the two considered cases. A total of six different realizations of the 100×100 network were generated, and the results of the simulations were compared. From the comparison of the two figures, it is clear that the variations in the m_e versus t curves for the exposed small-pore case are much higher than the exposed large-pore case. The former displays a large variation in the initial slopes of the almost-linear curves that abruptly change slope to yield a set of almost parallel final curves at larger times. On contrary, the exposed large pore m_e versus t curves show the typical decay pattern characteristic of the homogeneous networks, e.g. as seen in [22], and progressively merge into a single curve.

An explanation for the singular set of parallel curves obtained in Fig. 6A is in order. As described in Appendix A.1, the diffusion-controlled mass-flux of water vapors through the network at large times is entirely dominated by the small-pore lower-layer (constant) properties and is independent of the large-pore upper-layer (time-dependent) properties. Incidentally, the mass-flux j is also equal to the rate at which liquid mass is evaporated, or the slope of the curves shown in Fig. 6A. Since the mass-flux j as described by Eq. (A.5) is a constant for the later-time evaporations, the slopes of all the evaporation curves for different realizations shown in Fig. 6A reduce to the same constant at larger times, and hence they are all parallel for $t > 1000$ h.

3.3. Comparison of evaporation curves for the two cases

We would now compare the evaporation history in terms of the evaporated mass versus time plots for the exposed large pore case (Case 1), and the exposed small-pores case (Case 2). Two extreme curves, which were observed in the study of scatter of such curves presented in Fig. 6 for the two cases, form the upper and lower bounds of the corresponding evaporation-rate envelops shown in Fig. 7. Despite the fact that the exposed small pores case has wider envelope due to a larger scatter, envelope of the exposed large pores case remains clear of the former. It is also clear that the evaporation rate (dm_e/dt or $\dot{m}_e$) for the exposed large pores case remain higher throughout-it is understandable since the larger pores means larger amount of water for evaporation as well as smaller diffusive resistance for the water vapor. The evaporation rate for the exposed small pore case is high in the beginning, but drops rather sharply later on and then remains almost a constant for the remainder of the time.

3.4. Effect of uniform porosities in the two layers

In the studies done till now, we have created large and small pores by changing the throat widths l shown in Fig. 1 while keeping the inter-pore or inter-nodal distance a as a constant 1 mm for the two regions in the 100×100 network (Table 1). So l is larger for bigger pores, while it is smaller for smaller pores. As a result, we have smaller "particles" in the big pore region and larger particles in the small-pore region. Another consequence is that the porosity also changes: it is bigger in the large pores region and smaller in the small-pore region. (Note that the porosity can be shown to be $\varepsilon = (1/a)(2 - 1/a)$ for the uniform network shown in Fig. 1. So the porosity lies in the range $0.91 < \varepsilon_L < 0.96$ for the large pore layer and in the range $0.19 < \varepsilon_S < 0.36$ for the small pore layer.) Consequently our network model creates a porous medium where the porosity varies with the particle size.

However in granular porous media composed of spherical glass beads or sand particles, the porosity typically does not vary with the particle size-the porosity is the same in porous media composed of large particles or the small particles, provided the packing arrangement is unchanged. In such media, the two layers with different sized particles will have the same pore volume, which also implies that the initial volume of water available for evaporation in the two layers is identical as well. It is also important to note that the vapor mass-flux through a network cross-section can be expressed as

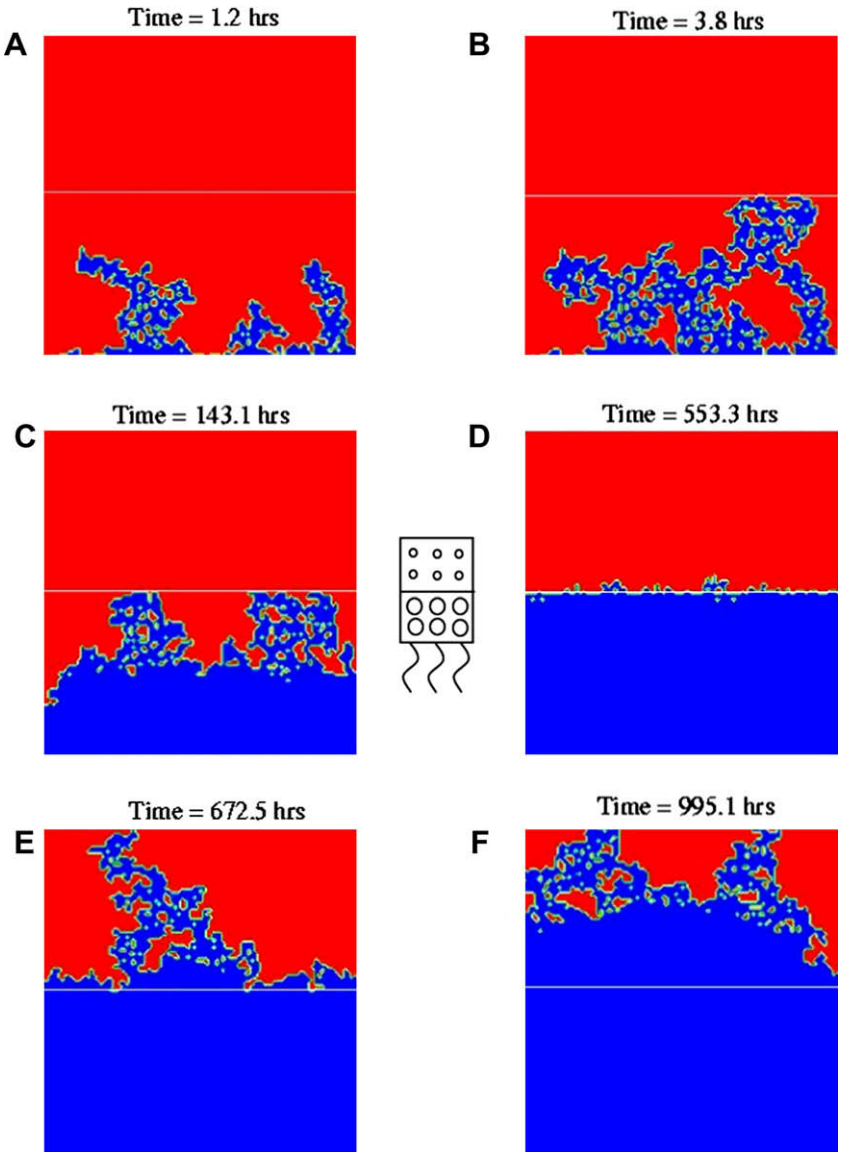

Fig. 5. A typical evolution of the drying of a 100 × 100 dual-porosity network with large pores in the exposed bottom layer. Evaporation happens at the bottom edge of the square; the other edges are sealed. Part (E) shows the state of pore saturation at the 'breakthrough'.

$$j = -\varepsilon D \frac{M_v}{RT} \nabla P_v \tag{3}$$

where ε is the cross-section area porosity and ∇P_v is the gradient of the vapor partial pressure. It is important to note that εD, which can be taken to be the effective network diffusion coefficient, will remain constant in the granular media irrespective of the particle size.

So in order to test the effects of constant porosity in our two-layer network, we artificially fix the porosity of the two layers to be the same. (A value of $\varepsilon = 0.75$ was assigned as the uniform network porosity, which results from taking the throat width l to be half of the inter-pore distance a, Fig. 1. Note that this porosity lies between the porosities of the large-pore and small-pore layers given earlier.) As a result, the volume of liquid to be evaporated in the two layers as well as the effective network diffusion coefficient εD remain identical in the two layers of this special 'granular' porous media with different pore sizes. (This situation is different from our regular two-layer network that will have a higher εD in the large pores region.) However the pore-size distributions in the two layers remain unchanged for application of the invasion percolation algorithm and are identical to the ones considered in Sections 3.1.1 and 3.1.2. This means that the invasion patterns are exactly identical to those shown in Figs. 3 and 5 (but not at the times indicated in these figures since the pore network effective diffusion coefficient as well as the overall mass to be evaporated are different).

First we study the exposed large pores case. Parts (a) and (b) of Fig. 8 describe the early-time and later-time plots of saturations of the two layers and the overall network. We see in part (a) that initially only the bottom-layer saturation changes and is the cause of the decline of the overall saturation, while the top-layer saturation holds constant. This trend continues till around 600 h [part (b)], when the bottom-layer saturation goes to zero, and then we see a decline in the top-layer saturation. This trend reflects the pattern seen in the drying evolution described in Fig. 5: large pores in the bottom have to dry up first in order for the small pores at the top to start drying. Part (c) of Fig. 8, which plots the number of clusters lying across the middle boundary as a function of drying time, shows that there is one single cluster till around 600 h, and none after that. So this plot also matches the trend seen in 5. Incidentally the time of 600 h corresponds to the 'transfer' of the drying front

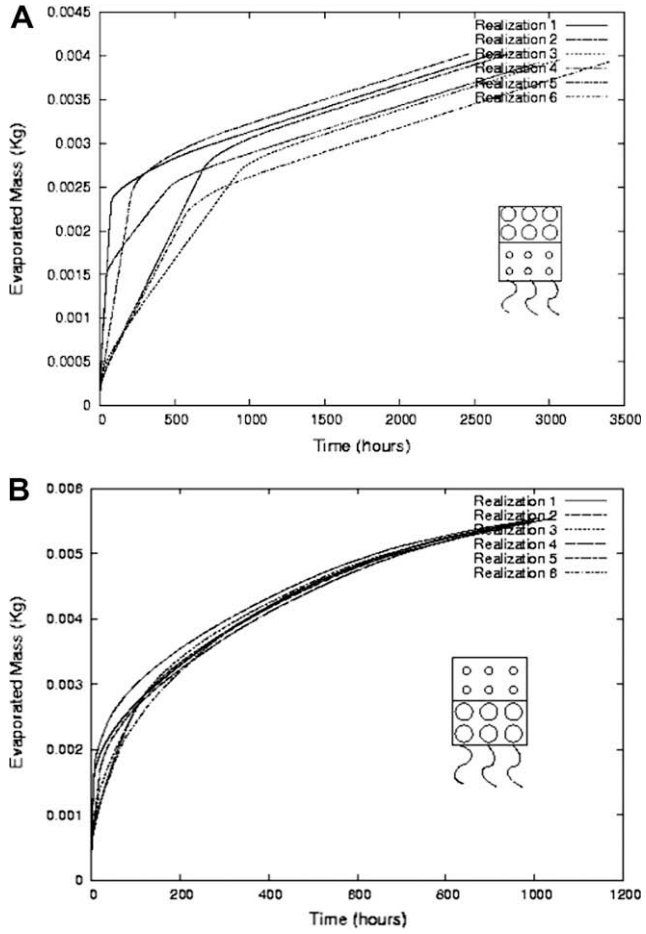

Fig. 6. Evaporated mass versus time plots for six realizations of the 100×100 dual-porosity network for (A) the exposed lower layer made of smaller pores, (B) the exposed lower layer made of larger pores.

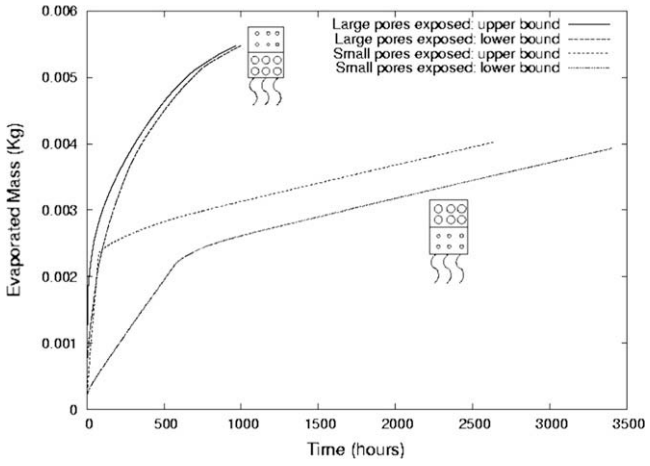

Fig. 7. A comparison of the evaporated mass versus time plots for the exposed small pores and the exposed large pores cases of 100×100 dual-porosity network. The two bounds in each case represent approximately the envelope within which most of the curves from different realizations are expected to fall.

from the lower layer to the upper layer when the drying front reaches the middle boundary while ensuring the complete evaporation of all the remaining lower-layer clusters.[1] So at this 'transfer' time, the lower-layer saturation drops to zero and the upper-layer saturation starts its decline from the value of unity.

Let us now consider the exposed small pores case. Parts (a) and (b) of Fig. 9 describe the early-time and later-time plots of saturations of the two layers and the overall network. While studying it, let us keep the evaporation pattern described in Fig. 3 in mind. There we see that after the drying front reaches the middle boundary, it immediately crosses over to the upper layer. (So in this case,

[1] Note that the 'transfer' time will not be the same as the 'breakthrough' time for the lower layer in the traditional sense when the drying front just touches the middle boundary; the former is much higher than the latter.

Table 1
Values of fluid properties and network parameters used in the 100×100 network simulations.

Water density (kg/m^3)	1000.0
Air density (kg/m^3)	1.2
Molecular mass M_v of water (kg/kmol)	18
Ideal gas constant R (J/(K kmol))	8314.5
Equilibrium water-vapor pressure at 27 °C (Pascals)	3652.0
External (film) transfer length scale δ (m)	1.0E−4
Inter-pore distance a (m)	1.0E−3
Network thickness (m)	1.0E−3
Occupancy coefficient β	0.46

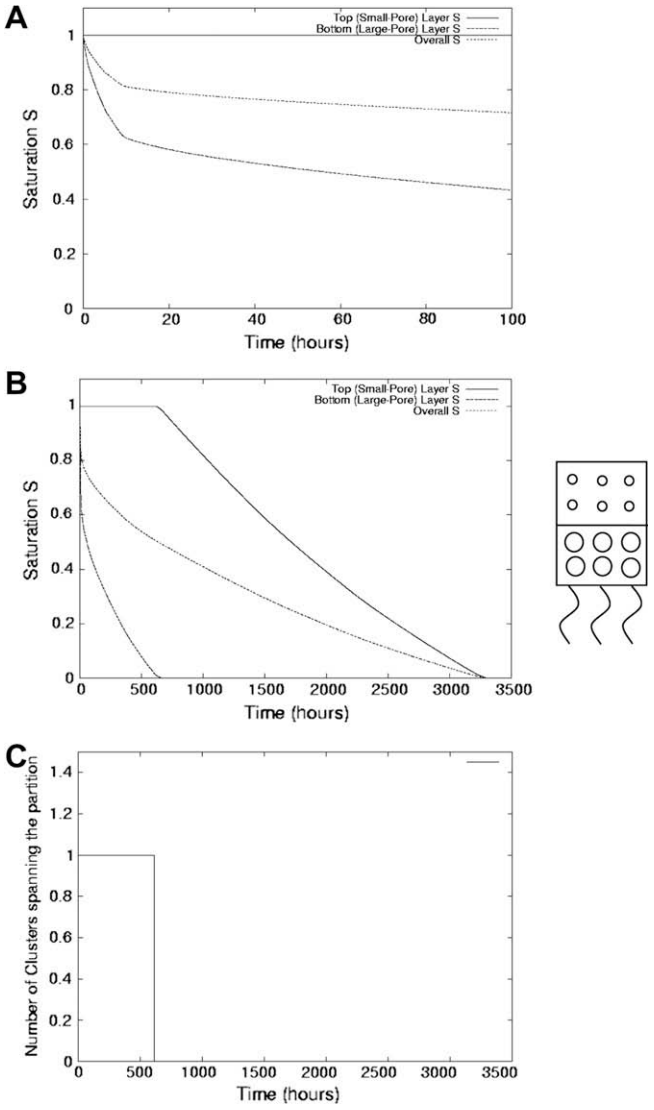

Fig. 8. Effect of imposing the constant-porosity condition in 100×100 dual-porosity network with large pores in the exposed bottom layer. Part (A): early-time evolution of the saturations of the two layers and the overall network. Part (B): later-time evolution of the same saturations. Part (C): change in the number of liquid clusters lying across the middle interface with time.

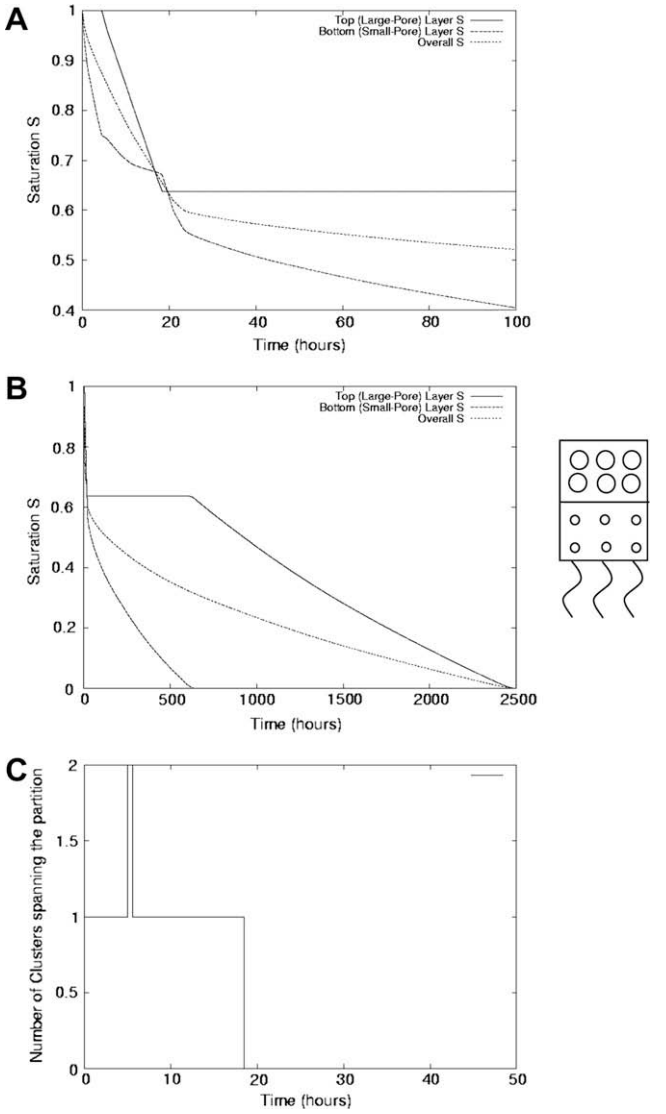

Fig. 9. Effect of imposing the constant-porosity condition in 100×100 dual-porosity network with small pores in the exposed bottom layer. Part (A): early-time evolution of the saturations of the two layers and the overall network. Part (B): later-time evolution of the same saturations. Part (C): change in the number of liquid clusters lying across the middle interface with time.

the lower-layer breakthrough time and the transfer time are identical.) We also note that after the breakthrough in the lower layer, not much change happens in the shape of the drying front in the lower layer. However there is a veritable explosion of vapor-occupied pores in the upper layer due to the 'pumping' of water from the upper layer pores to the lower layers. This phenomenon is reflected in the saturation curves as well. The early-time decline in the lower-layer saturation is arrested a bit at 7 h which corresponds to the breakthrough time in the lower layer. This fact is validated by part (c) of Fig. 9: the single liquid-cluster lying across the boundary layer breaks up into two at around 7 h due to the passage of the drying front. After this lower-layer breakthrough, the upper-layer saturation in part (a) begins to show a sharp decline as result of the pumping action described above. After around 20 h, the decline in the upper-layer saturation stops abruptly, and it remains constant till about 600 h, during which the lower-layer saturation reduces to zero. During this constant-saturation phase, the shape of the drying front in the upper layer is expected to remain unchanged, as shown by parts (d) and (e) of Fig. 3. The drying of upper layer initiates after the lower layer is completely dry. Note that the drying rate of upper layer (as characterized by the slope of the saturation curve) is much lower than the rate for the lower layer—this is due to the large diffusive resistance experienced by vapors while traversing the whole depth of the empty lower layer (Fig. 3f).

It is also interesting to note that the overall saturation in this study will be the arithmetic mean of the saturations for the two layers—this fact easily verified by studying parts (a) and (b) of Figs. 8 and 9.

Since the invasion patterns are identical to those considered in Sections 3.1.1 and 3.1.2, the evolutions of saturations described in this section also apply qualitatively to the cases with non-uniform porosity. The impact of the uniform porosity lies in the drying kinetics and is analyzed in the next section.

3.4.1. Comparison of the same-porosity evaporation curves with those for different porosities in the two layers

Evaporated mass as a function of time is plotted for the constant porosity case in Fig. 10. Based on our earlier studies in Section 3.2 on the scatter of such curves due to pore-structure variation induced due to different network realizations, we developed an envelope that is likely to include most possible curves for each case by considering two extreme curves as its bounds. Part (A) of the figure plots curves for the exposed small pores case, while part (B) addresses the opposite case.

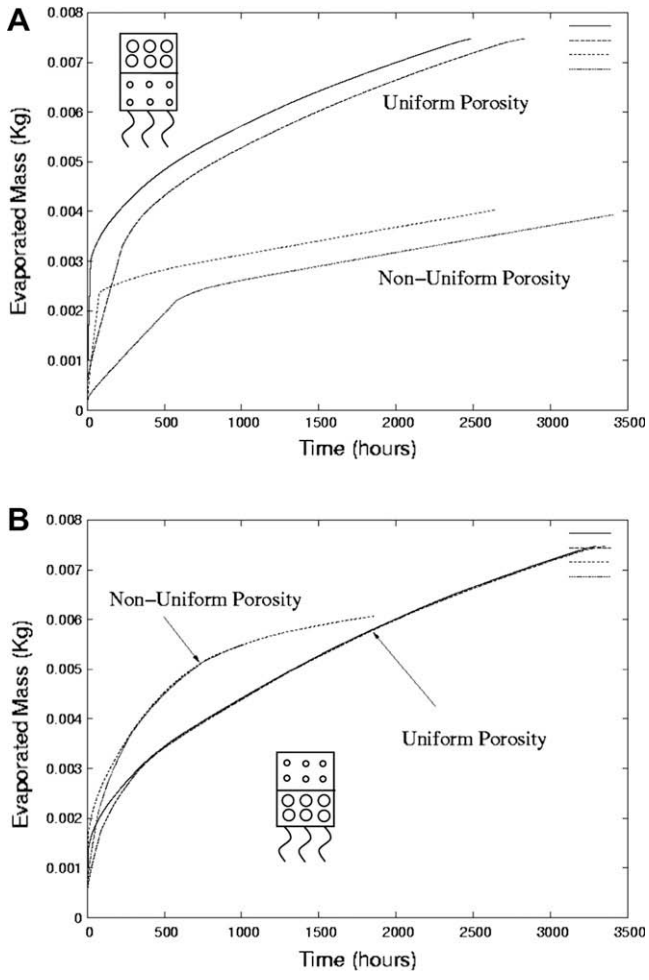

Fig. 10. Comparing the effect of uniform and non-uniform porosities in the two layers upon the evaporation plots: (A) exposed small pore case; (B) exposed large pore case. Two different, extreme realizations were considered in the uniform and non-uniform porosity situations for capturing the effect of pore-structure variations on evaporation rates.

We see clearly that when the small pores are in the bottom, the uniform porosity case has much higher evaporation rate. Moreover its curves no longer have the striking bilinear nature, characteristic of the curves corresponding to the earlier considered, non-uniform porosities case. An explanation for the appearance of 'bilinearity' in such curves was provided with the help of Appendix A.1 in Section 3.2. A similar explanation for the lack of bilinearity in the uniform porosity evaporation curves is presented in Appendix A.2. This implies that a two-layer media created from spherical beads of two different sizes will not only have a higher evaporation rate than a dual-porosity porous medium, but its large-time evaporation rate will also not remain constant.

Let us now consider the case of large pores in the bottom in Fig. 10B. Here, we see a reversal in the trend: the non-uniform porosity network has higher evaporation rate as compared to the uniform porosity network. We also observe that the possible variations in the curves due to different network realizations are also very less, as evident in the very narrow envelope of curves for the two porosity distributions. Moreover both types of curves follow the general exponentially decaying trend of the evaporation curves shown earlier in Fig. 6B.

Note that the evaporation curves shown in Fig. 10 indicate that the uniform porosity networks have a higher evaporation rates as compared to the exposed small pore case, but have a lower rate as compared to the exposed large pore case. This can be explained in terms of the assigned porosities. Since the vapor mass-flux $j \propto \varepsilon$ as in Eq. (3), and since the uniform porosity lies between the large pore and small pore porosities, we can clearly see that initial slopes of the evaporation curves follow the porosity values of the lower, exposed layers.

3.5. Comparison with experiments

A comparison of our network simulation predictions with observations of evaporation in a real experiment was sought to improve confidence in the results obtained from the network simulation. A smaller 12×12 network was considered for this study and water was used as the working fluid.

3.5.1. Description of experimental setup

Fig. 11 describes the experimental setup used for studying the 12×12 network during its drying. The network was machined into a plexiglas base plate while its top was covered by a transparent sheet of RTV. The network was placed on a platform which in turn

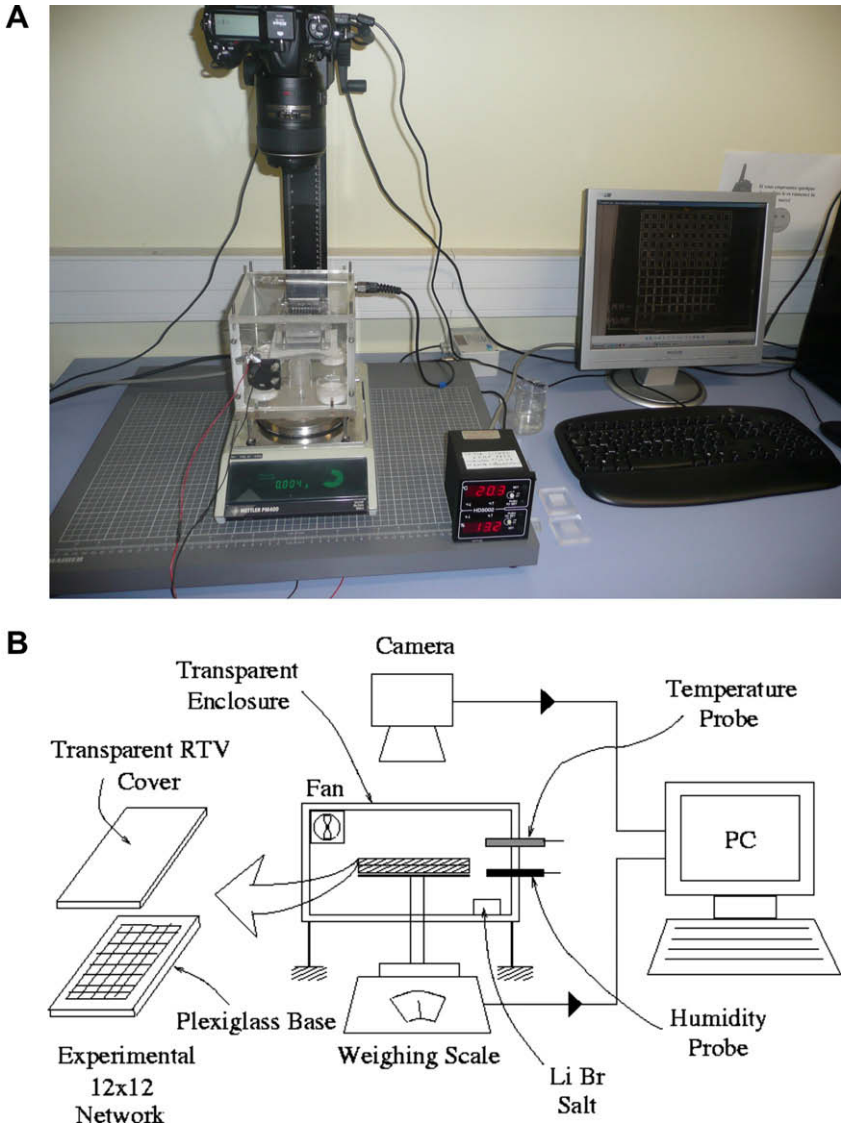

Fig. 11. (A) A picture of the experimental setup. (B) A schematic describing elements of the setup.

was resting on an electronic weighing scale. A transparent enclosure was built around the network to control the conditions of the surrounding air. The air humidity was monitored with a humidity probe while the relative humidity was kept close to 6% with the help of the hygroscopic Lithium Bromide (Li Br) salt. A small fan inside the enclosure recirculated air and helped us to maintain constant humidity everywhere within the enclosure. The air temperature was monitored with the help of a temperature probe and was found to be close to 20 °C during the experiments. Images of the network during drying were captured through a camera and were stored in a PC. The output from the weighing scale (resolution: 10^{-4} g) was stored in the PC as well.

3.5.2. Initial preparation for simulation

Owing to the machining precision, which was equal to 10 μm, it was not possible to select randomly the throat widths according to a continuous distribution as in the 100 × 100 simulations. We had to use a discrete random distribution. As a result, it might have happened that two or more equal width throats lie on the invasion front. In the experiments, these throats were never strictly of equal width due to machining uncertainties. This might have been be a source of discrepancy between the experiment and the simulation as it may then would have been impossible to anticipate the throat that would eventually be invaded in the experiment. In order to minimize this effect, we constructed the experimental network such that this equal width throat choice problem does not occur (this was only possible for small networks and was achieved by testing numerically several realizations using the square network model of drying until one obtains a network where all interfacial throats differ in width, within the machining accuracy, at any stage of drying).

The convective mass transfer coefficient (h) used for evaporative liquid mass-loss at the lower exposed edge of the 12 × 12 network was used for experimental validation. Note that at the network edge, we used h in the mass-flux boundary condition of the form

$$j = \varepsilon h(P_{v,o} - P_{v,\infty}) \quad \text{where} \quad h = \frac{D}{(R/M_v)T\delta} \tag{4}$$

The second part of the above equation becomes self-evident on comparing the first part with Eq. (1). Here δ is the width of the boundary film over which the mass transfer is taking place. In our simulations, the value of δ as listed in Table 1 was taken to be a fixed constant. However in order to estimate δ for the 12 × 12 networks during this comparison, we matched the mass evaporation rate m_e at the start of the experiment (obtained from the $t = 0$ slope of the mass evaporation curves shown in Fig. 14 for the experiments) with the one given as

$$\dot{m}_e = \frac{P_{atm}D}{\left(\frac{R}{M_v}\right)T\delta} \ln\left(\frac{P_{atm} - P_{v,\infty}}{P_{atm} - P_{v,0}}\right) \tag{5}$$

which allowed us to compute δ for the two cases. Here P_{atm} is the atmospheric pressure. Eq. (5) (derived from Eq. (18.2–14) of [26]) assumes that at the start of the experiment, there is only a stationary film of air of thickness δ that lies between water surface at the edge of the fully saturated network and the surrounding ambient, and there is only diffusion of water vapor through this film during this initial evaporation. The thermodynamic properties were estimated at the enclosure temperature of 20 °C and the ambient vapor pressure $P_{v,\infty}$ corresponded to the relative humidity of 6% maintained inside the enclosure.

3.5.3. Comparing experimental results with predictions by simulation

We will compare the predictions of our simulation with experiments at certain distinct events which can be called milestones during the evaporation of the two types of two-layer networks.

Let us first consider the exposed large pores case of the 12 × 12 network. Fig. 12 shows the distribution of air and water phases during drying for both the simulation and the experiment. A good validation of the drying pattern is provided by parts A2 and B2 of the figure which show the half-way point in the evaporation process-it is heartening to see that the preferential drying of the outer lying larger pores ahead of the smaller inner pores (as predicted by our earlier 100 × 100 network simulation as well) happens in the nature too. We also studied the saturation distribution during the breakthrough of the air phase to the opposite face of the rectangular domain. Parts A3, B3 of Fig. 12 show a striking correspondence in the breakthrough patterns created by the simulation and experiment, once again highlighting the remarkable ability of the invasion percolation algorithm to recreate the natural drying patterns. We also note that the form of the evaporation curve is replicated quite well by the simulation in Fig. 14A.

However, there are a few areas where the weakness of our network simulation is evident. For example, the simulation seems to have faltered in predicting the initial drying of the network in the large-pore region at the first milestone when the air phase first reaches the middle interface—little similarity can be found in the saturation distributions of parts A1 and B1 of Fig. 12. Similarly, the dimensionless times for the initial and half-way point saturation distributions do not match also (though there is a reasonably good match of t^* for the breakthrough point). This difference in the drying times can be attributed to the observed difference in the time taken to dry the network completely: T_{dry} is 134.167 h for the simulation while it is merely 31 h in the experiments. So a large difference in the drying times of the network as predicted by the simulation and as seen in the experiment is rather worrisome.

Let us now consider the exposed small pores case of the 12 × 12 network. A comparison of distributions of air and water phases during drying, as predicted by the simulation and as observed during experiments, is presented in Fig. 13. Unlike the first case, we do see a rather good validation of the initial touching of the middle interface event predicted by the simulation in parts A1 and B1 of the figure. Let us next consider the breakthrough of air phase onto the end of the network, as shown in parts A2 and B2 of Fig. 13. The draining of the upper, larger-pore region caused due to the capillary pumping phenomenon, as described in Section 3.1.1, is displayed both by the simulation as well as the experiment. Note that the dimensionless time taken to reach this second milestone is fairly well predicted by the simulation. On comparing the evaporation rates in Fig. 14B, we once again note that the form of the evaporation curve is replicated quite well by the simulation. It was very encouraging to see that the bilinear evaporation curves, predicted by earlier simulations as well, do actually occur in nature!

Coming to the weaknesses of the simulation, we observe that the patterns of drainage shown in parts A2 and B2 are different. We also notice that parts A3 and B3 of Fig. 13, which represent the milestone of complete drainage of the larger pores, the experimental phase distribution is never replicated by the simulation. (B2 and B3 show that while the big pores are getting completely drained, the saturation pattern of smaller pores remains unchanged. As seen in part A3, the IP algorithm of the simulation is unable to replicate the complete drainage of the big pore region.) Another disconcerting fact about this simulation is that the predicted drying time is much larger than the one seen for the experiment.

3.5.4. Explanation of discrepancies and future work

We would like to offer some explanation for this big difference in drying times. The reason for the simulation network to take longer to dry completely can be explained as follows. One of the

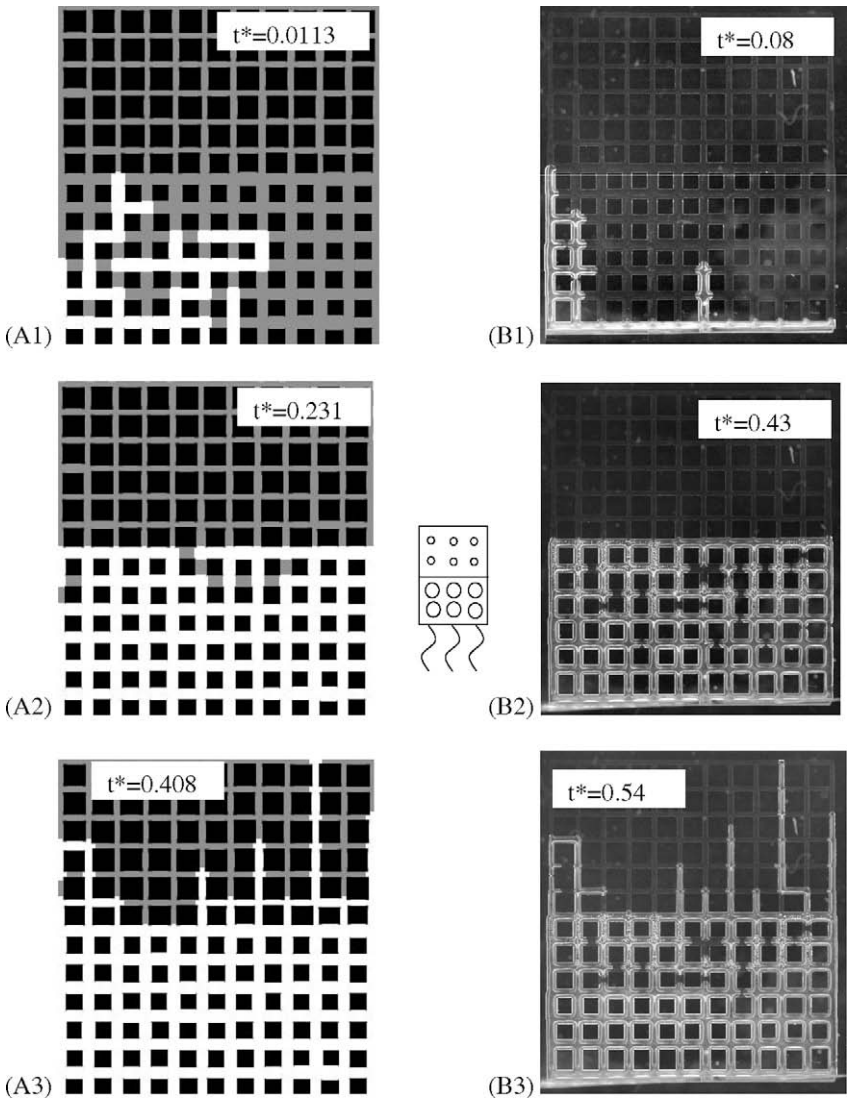

Fig. 12. Comparison of numerical prediction with experimental result for drying in a 12 × 12 dual-porosity network with large pores in the exposed bottom layer. (A3) and (B3) shows the state of pore saturation at the 'breakthrough'. Dimensionless time $t^* = t/T_{dry}$ with T_{dry} = 134.167 h for the simulation, and T_{dry} = 31 h for the experiment.

novel phenomena observed during the experiments was the presence of liquid films left behind by the retreating water during evaporation. These films of liquid on the inside of the top cover plate of the experimental network were often accompanied by tiny droplets, especially in the larger pores drained by capillary pumping in the exposed small pore case where the relative humidity of air could not be controlled that effectively. (For example, these droplets can be seen as the faintly visible small dots in the empty large pores in part B3, Fig. 13.)

Incidentally such films are different from films at the channel corners of the square network that have already been modeled and incorporated in the drying simulations [11]. (As reported in [27], the contact angle of liquid water on a plexiglas surface is close to 80° whereas the critical contact angle above which the corner films do not form in channels of rectangular cross-section is 45° [11].) In contrast to these "thick" films, thin films of a few nanometres thickness can develop on a smooth surface [28]. However, transport in such thin films plays a role only in very small pores because of their very low hydraulic conductivity. Furthermore, the high contact angle of 80° definitively does not favour formation of thin films. In a previous work on imbibition in networks of similar geometry [29], films at a scale smaller than the corner films were also considered and were referred to as roughness films. In the present case, these films are thought to develop along the microgrooves resulting from the machining process. Like the corner films, the flow in roughness films is driven by capillarity. Therefore, we believe that the films seen in our experiment can be referred to as the roughness films.

We believe that presence of such roughness films significantly reduces the actual drying time, and is responsible for the big discrepancy in the total drying times for the simulations and experiments. This film effect may be similar to the films seen on the surface of rough particles during drying, and therefore it is worth our while to model such phenomenon. In future, we plan to study such surface films in greater detail, develop relevant physics to model it, and then incorporate it in the 2-D network drying simulation. However as a final remark, we note that the effect of roughness films is probably more enhanced in the small machined network with fewer pores for the experiment—such effects may not be significant in larger networks that are closer to the 'real' porous media. So the behavior of our earlier simulation in a larger network without the film effect may not be far from the behavior of real systems.

We would also like to comment on another new phenomenon observed in the experiments. For the exposed small pores case, it was found that at the point when a finger of dried air channel

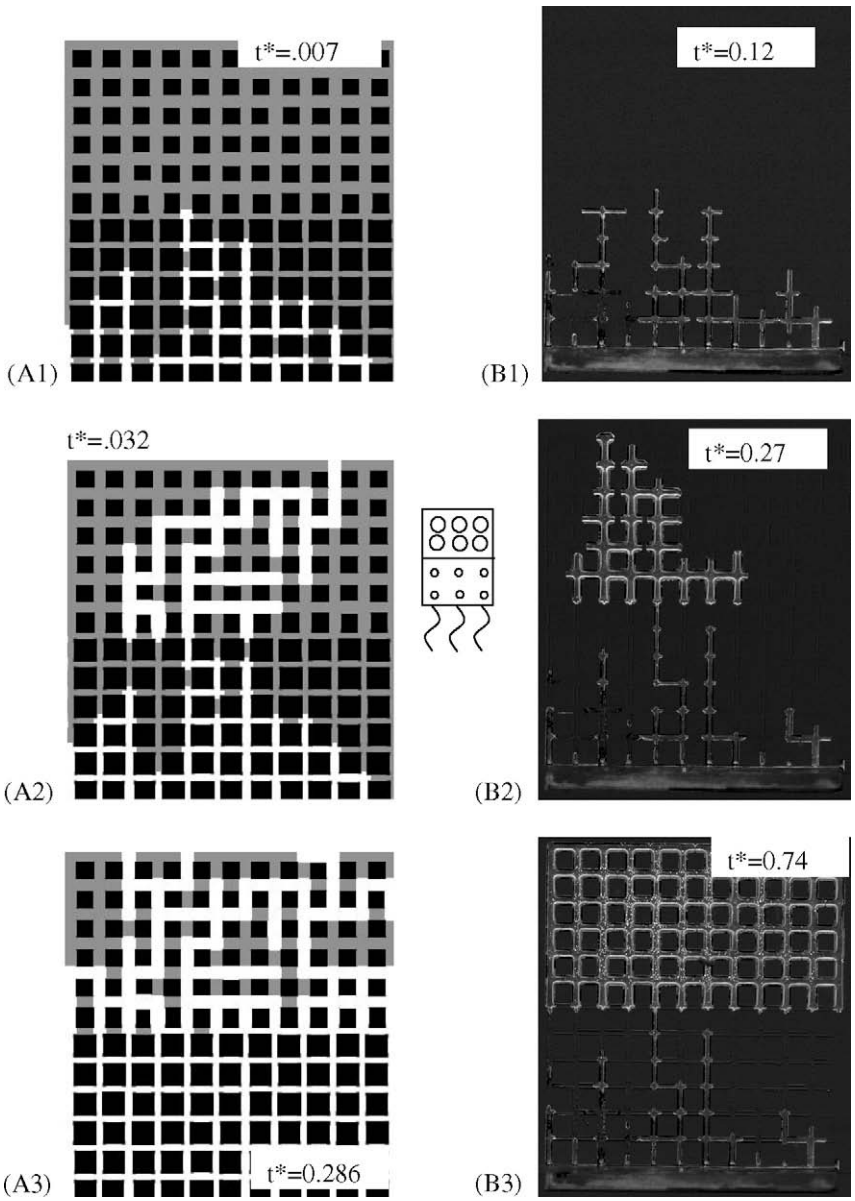

Fig. 13. Comparison of numerical prediction with experimental result for drying in a 12 × 12 network with small pores in the bottom layer and large pores in the top layer. (A2) and (B2) shows the state of pore saturation at the 'breakthrough'. Dimensionless time $t^* = t/T_{dry}$ with $T_{dry} = 148.80$ h for the simulation, and $T_{dry} = 14.16$ h for the experiment.

touched the larger pores at the top at the middle interface (B1 of Fig. 13), some amount of liquid traveled from larger pores to the smaller pores as a result of capillary suction. This might be viewed as 'redistribution' of liquid from large pores to small pores. The time scale for such redistribution was observed to be much smaller than the time scale associated with drying.[2] Note that this 'capillary suction' effect is different from the 'capillary pumping' effect discussed earlier in Section 3.4 with Fig. 4: the latter is the result of applying the IP algorithm that is based on drainage of liquids during drying, while the former is an entirely new, imbibition like effect seen in the drying of a dual-porosity network and is presently outside the scope of the IP algorithm.

As a final remark, we note that the IP model can also be questioned in systems of high contact angle approaching 90° from below [30]. As discussed more recently in [31] also, more refined invasion rules have then to be used owing to the occurrence of cooperative effects between growing menisci.

Thus, we believe that these effects are behind the rather less than satisfactory prediction of last stage of network drying, i.e. for example the big difference in A3 and B3 of Fig. 13. There we observe that the complete drainage of large pores before smaller pores are drained is not predicted by the simulation. So more work remains to be done in future for incorporating these effects in the drying model.

4. Summary and conclusion

The evaporation of water from a two layer heterogeneous medium with two different pore sizes was studied with the help of a square 100 × 100 network. The pattern of evaporation for the cases of exposed small pores and exposed large pores lead to dramatically different patterns and evaporation curves. For the case of

[2] Incidentally in a drying experiment conducted with ethanol on the same network, this redistribution effect was found to be much more dramatic and periodic in nature. More of this will be discussed in a future publication.

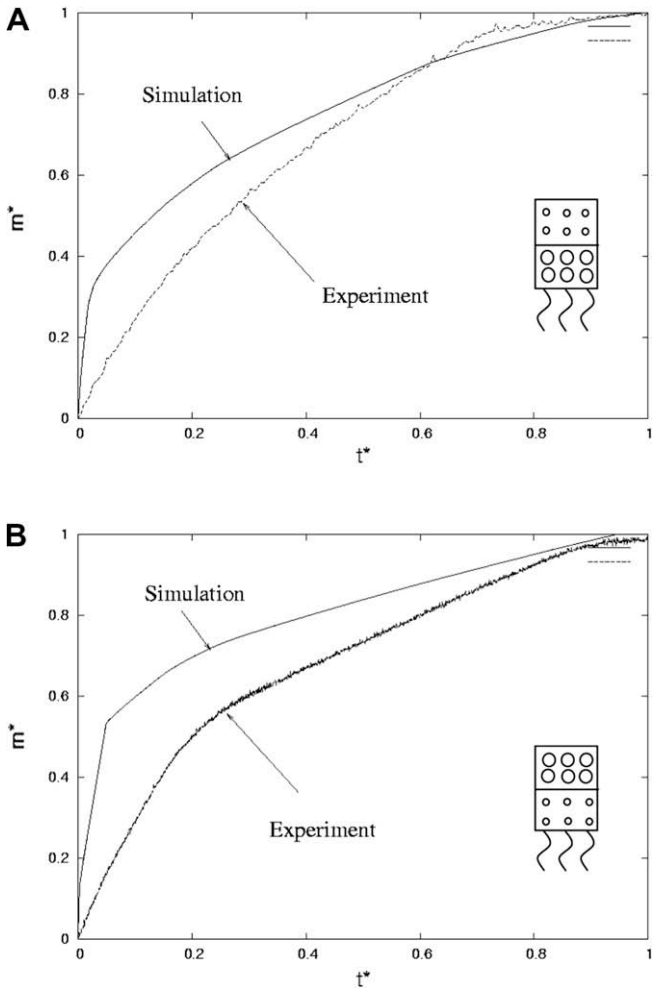

Fig. 14. Comparison of numerical prediction with experimental result for drying in a 12 × 12 network. The evaporated mass is normalized with the net mass of liquid evaporated from the network at the end of complete drying, i.e. $m^* = m/m_{dry}$. Similarly dimensionless time $t^* = t/t_{dry}$. (A) Exposed large pores: with $t_{dry} = 134.167$ for the simulation, and $t_{dry} = 31$ h for the experiment, where $m_{dry} = 4.3563\,\mathrm{E}{-4}$ kg for the simulation and $m_{dry} = 3.44\,\mathrm{E}{-4}$ kg for the experiment. (B) Exposed small pores: here $t_{dry} = 148.80$ h for the simulation, and $t_{dry} = 14.16$ h for the experiment. Here $m_{dry} = 4.3563\,\mathrm{E}{-4}$ kg for the simulation and $m_{dry} = 5.10\,\mathrm{E}{-4}$ kg for the experiment.

exposed small pores, salient features of the evaporation process were a quicker breakthrough, drainage of the inner larger pores due to capillary pumping, and much wider envelope of the unusual bilinear evaporation curves. The case of exposed large pores was characterized by preferential evaporation of the outer larger pores, much slower breakthrough, and a much narrower envelope of the conventional exponential-type drying curves. Evaporation rates were found to be higher in the latter. Imposition of uniform porosity in the two layers led the bilinear evaporation curves for the exposed small pore case to acquire the regular decaying form; evaporation curves for the exposed large pore case were not affected that much. Experimental validation of the network simulation for a smaller 12 × 12 network for both cases revealed that important milestones of the evaporation process, including saturation distribution during breakthroughs, and preferential drying of larger pores, were replicated to a large extent by the simulation. Though the forms of the experimental evaporation curves were successfully replicated by the simulation as well, drying times were over-predicted. The causes of such divergences are mainly attributed to the presence of surface liquid films caused due to surface roughness. As a result, this film effect needs to be incorporated in the model to improve its accuracy. Our results also suggest that the more advanced drying models have to incorporate: (1) more refined invasion rules, as compared to the current simple IP rules, for systems of very high contact angle close to 90°; (2) the possible imbibition of water back into small pores from large pores during the drying of the exposed small pore network .

Acknowledgement

Financial support from CNRS (Centre National de la Recherche Scientifique), France is gratefully acknowledged.

Appendix A

A.1. Large-time mass-flux for the small-pore lower-layer network

Here, we will be estimating the diffusive flux of water vapors through the dried up portions of the exposed small-pore system in an attempt to explain the parallel evaporation curves observed at large times in Fig. 9A. From the study of part (f) of Fig. 3, it is clear that this phase of evaporation is marked by a completely dry small-pore lower layer and a partially progressed flat piston-like effective drying front in the large-pore upper layer. (The effective drying front is defined here as the curve marking the boundary of the still remaining clusters.) The conditions at this front can be approximated as that of the fully saturated air with 100% humidity, since the gaps between the still remaining clusters behind this front are quite small. A simplified drying model based on this approximation is shown in Fig. A1.

The diffusive mass-flux j of water vapors through the dried portions of the network can be expressed as

$$j = \varepsilon_L K \frac{P_{v,e} - P_{v,i}}{h} = \varepsilon_S K \frac{P_{v,i} - P_{v,\infty}}{H} \tag{A.1}$$

where $K = D\frac{M_v}{RT}$ and ε_L, ε_S are the area porosity of the network in the large- and small-pore layers, respectively. P_v is the partial pressure of water vapors with the subscripts e, i and ∞ refer to the conditions at the effective drying front, the two-layer interface, and the open air at the bottom of the network, respectively. After eliminating $P_{v,i}$, the two independent relations in Eq. (A.1) can be easily manipulated to obtain an intermediate relation

$$P_{v,e} - P_{v,\infty} = \frac{j}{K}\left(\frac{h}{\varepsilon_L} + \frac{H}{\varepsilon_S}\right) \tag{A.2}$$

which in turn yields the final expression for the mass-flux as

$$j = k \frac{P_{v,e} - P_{v,\infty}}{\frac{H}{\varepsilon_S}\left(\frac{h}{H}\frac{\varepsilon_S}{\varepsilon_L} + 1\right)} \tag{A.3}$$

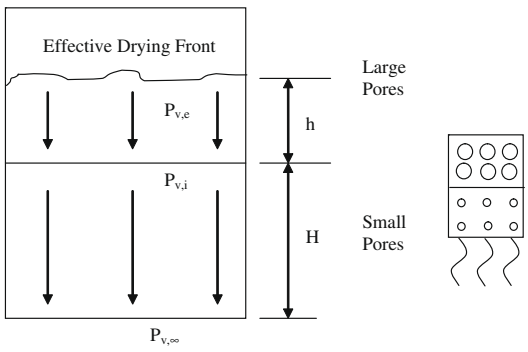

Fig. A1. A schematic describing the later-time evaporation in the exposed small-pores system after the lower layer has dried completely and a clear effective drying front can be discerned in the upper layer.

As is clear from Fig. 1, the area porosities ε_L and ε_S are proportional to the average throat widths: $\varepsilon_S \propto 0.15a$ since throat-width range is $0.1a \le l \le 0.2a$ in the small-pore layer; $\varepsilon_L \propto 0.75a$ since throat-width range is $0.7a \le l \le 0.8a$ in the large-pore layer. We can also see that the h is smaller than H in Fig. A1. Therefore one can surmise that

$$\frac{h}{H} < 1 \quad \text{and} \quad \frac{\varepsilon_S}{\varepsilon_L} \sim 0.2 \Rightarrow \frac{h\varepsilon_S}{H\varepsilon_L} << 1 \tag{A.4}$$

As a result, the expression for mass-flux reduces to

$$j = \varepsilon_S K \frac{P_{v,e} - P_{v,\infty}}{H} \tag{A.5}$$

So the diffusive mass-flux is independent of the upper (large pore) layer properties ε_L and $h(t)$, and is entirely decided by the lower (small pore) layer properties ε_S and H. This stands to reason because the diffusion of water vapors from the effective drying front to the exposed network edge has to face the diffusive resistances inside large pores over the time-dependent length h and inside small pores over the constant length H, respectively. (These resistances can be thought of as being 'in series'.) Analysis of Eq. (A.4) indicates that due to its large pores, the resistance offered by the upper layer is insignificant compared to the lower layer resistance, and hence it is neglected in the expression for mass-flux (A.5).

A.2. Effect of uniform, constant porosity on the large-time mass-flux for the small-pore lower-layer network

Here we will explain the difference in evaporation curves observed in Fig. 10A at large times after the implementation of uniform porosity in the upper and lower layers. As discussed in Section 3.4.1, the uniform porosity curve is gently sloping at large times, unlike the parallel curves for the non-uniform porosity case. So let us look at the expression for diffusive mass-flux j in the dried up part of the network which is given in Eq. (A.3). For the uniform porosity case, the area porosities ε_L and ε_S for the large and small pore layers, respectively, are equal to each other, and are each of the value let us say ε In that case, (A.3) reduces to

$$j = \varepsilon K \frac{P_{v,e} - P_{v,\infty}}{H + h} \tag{A.6}$$

So unlike (A.5) and (A.6) has $(H + h)$ in the denominator, and which implies that the mass-flux j decreases with time as the distance h of the effective drying front from the middle interface increases during drying. This fact explains the declining slope of the uniform porosity evaporation curve with time.

References

[1] S. Whitaker, Simultaneous heat, mass and momentum transfer in porous media. A theory of drying, Advances in Heat Transfer, vol. 13, Academic Press, New York, 1977, pp. 119–203.
[2] M. Prat, Recent advances in pore-scale models for drying of porous media, Chem. Eng. J. 86 (1–2) (2002) 153–164.
[3] T. Metzger, E. Tsotsas, M. Prat, Pore network models: a powerful tool to study drying at the pore level and understand the influence of structure on drying kinetics, in: A. Mujumdar, E.T. Tsotsas (Eds.), Modern Drying Technology, vol. 1, Computational Tools at Different Scales, Wiley, 2007, pp. 57–102 (Chapter 2).
[4] M. Prat, Percolation model of drying under isothermal conditions in porous media, Int. J. Multiphase Flow 19 (4) (1993) 691–704.
[5] M. Prat, Isothermal drying of non-hygroscopic capillary-porous materials as an invasion percolation process, Int. J. Multiphase Flow 21 (5) (1995) 875–892.
[6] A.G. Yiotis, A.K. Stubos, A.G. Boudouvis, Y.C. Yortsos, A 2-D pore-network model of the drying of single-component liquids in porous media, Adv. Water Resour. 24 (2001) 439–460.
[7] H.P. Huinink, L. Pel, M.A.J. Michels, M. Prat, Drying processes in the presence of temperature gradients. Pore-scale modelling, Eur. Phys. J. E 9 (2002) 487–498.
[8] F. Plourde, M. Prat, Pore network simulations of drying of capillary media. Influence of thermal gradients, Int. J. Heat Mass Transfer 46 (2003) 1293–1307.
[9] V.K. Surasani, T. Metzger, E. Tsotsas, Consideration of heat transfer in pore network modelling of convective drying, Int. J. Heat Mass Transfer 51 (2008) 2506–2518.
[10] A.G. Yiotis, A.G. Boudouvis, A.K. Stubos, I.N. Tsimpanogiannis, Y.C. Yortsos, The effect of liquid films on the drying of porous media, AiChE J. 50 (11) (2004) 2721–2737.
[11] M. Prat, On the influence of pore shape contact angle and film flows on drying of capillary porous media, Int. J. Heat Mass Transfer 50 (2007) 1455–1468.
[12] D.S. de Freitas, M. Prat, Pore network simulation of evaporation of a binary liquid from a capillary porous medium, Transport Porous Media 40 (2000) 1–25.
[13] Y. Le Bray, M. Prat, Three dimensional pore network simulation of drying in capillary porous media, Int. J. Heat Mass Transfer 42 (1999) 4207–4224.
[14] L.A. Segura, P.G. Toledo, Pore-level modeling of isothermal drying of pore networks. Effects of gravity and pore shape and size distributions on saturation and transport parameters, Chem. Eng. J. 111 (2005) 237–252.
[15] A.G. Yiotis, I.N. Tsimpanogiannis, A.K. Stubos, Y.C. Yortsos, Pore-network study of the characteristic periods in the drying of porous materials, J. Colloid Interface Sci. 297 (2006) 738–748.
[16] A.G. Yiotis, I.N. Tsimpanogiannis, A.K. Stubos, Y.C. Yortsos, Coupling between external and internal mass transfer during drying of a porous medium, Water Resour. Res. 43 (2007) W06403.
[17] J.B. Laurindo, M. Prat, Numerical and experimental network study of evaporation in capillary porous media Phase distributions, Chem. Eng. Sci. 51 (23) (1996) 5171–5185.
[18] J.B. Laurindo, M. Prat, Numerical and experimental network study of evaporation in capillary porous media. Drying rates, Chem. Eng. Sci. 53 (12) (1998) 2257–2269.
[19] I.N. Tsimpanogiannis, Y.C. Yortsos, S. Poulou, N. Kanellopoulos, A.K. Stubos, Scaling theory of drying in porous media, Phys. Rev. E 59 (4) (1999) 4353–4365.
[20] M. Prat, F. Bouleux, Drying of capillary porous media with stabilized front in two-dimensions, Phys. Rev. E 60 (5) (1999) 5647–5656.
[21] T.M. Shaw, Drying as an immiscible displacement process with fluid counterflow, Phys. Rev. Lett. 59 (15) (1987) 1671–1674.
[22] O. Chapuis, M. Prat, Influence of wettability conditions on slow evaporation in two-dimensional porous media, Phys. Rev. E. 75 (1–11) (2007) 046311.
[23] T. Metzger, A. Irawan, E. Tsotsas, Influence of pore structure on drying kinetics: a pore network study, AIChE J. 53 (12) (2007) 3029–3041.
[24] J.B. Laurindo, M. Prat, Modeling of drying of capillary porous media. The discrete approach, Drying Technol. 16 (9–10) (1998) 1769–1787.
[25] T. Lombardo, S. Simon, Desalination by poulticing: laboratory study on controlling parameters, in: 10th International Congress on Deterioration and Conservation of Stone, ICOMOS Sweden, Stockholm, 2004, pp. 323–330.
[26] R.B. Bird, W.E. Stewart, E.N. Lightfoot, Transport Phenomena, second ed., Wiley, 2002.
[27] N. Sghaier, M. Prat, S. Ben Nasrallah, On the influence of sodium chloride concentration on equilibrium contact angle, Chem. Eng. J. 122 (2006) 47–53.
[28] N.V. Churaev, Liquid and vapour flow in porous bodies: surface phenomena, Topics in Chemical Engineering, vol. 13, Springer, Berlin, 2000.
[29] R. Lenormand, C. Zarcone, Role of roughness and edges during imbibition in square capillaries, Society of Petroleum Engineers No. 13264, in: Proc. 59th Ann. Tech. Conf. SPE. Houston TX, USA.
[30] M. Cieplak, M.O. Robbins, Influence of contact angle on quasistatic fluid invasion of porous media, Phys. Rev. B 41 (1990) 508–521.
[31] O. Chapuis, M. Prat, M. Quintard, E. Chane-Kane, O. Guillot, N. Mayer, Two-phase flow evaporation in model fibrous media. Application to the gas diffusion layer of PEM fuel cells, J. Power Sour. 178 (2008) 258–268.